PAPER

Check for updates

Structural, magnetic and hyperthermia properties and their correlation in cobalt-doped magnetite nanoparticles†

L. T. H. Phong,[ab] D. H. Manh, [ID] *[ab] P. H. Nam,[a] V. D. Lam,[b] B. X. Khuyen,[a] B. S. Tung,[a] T. N. Bach,[a] D. K. Tung,[a] N. X. Phuc,[c] T. V. Hung,[d] Thi Ly Mai, [ID] [e] The-Long Phan[f] and Manh Huong Phan [ID] [g]

Cobalt doped magnetite nanoparticles ($Co_xFe_{3-x}O_4$ NPs) are investigated extensively because of their potential hyperthermia application. However, the complex interrelation among chemical compositions and particle size means their correlation with the magnetic and heating properties is not trivial to predict. Here, we prepared $Co_xFe_{3-x}O_4$ NPs ($0 \leq x \leq 1$) to investigate the effects of cobalt content and particle size on their magnetic and heating properties. A detailed analysis of the structural features indicated the similarity between the crystallite and particle sizes as well as their non-monotonic change with the increase of Co content. Magnetic measurements for the $Co_xFe_{3-x}O_4$ NPs ($0 \leq x \leq 1$) showed that the blocking temperature, the saturation magnetization, the coercivity, and the anisotropy constant followed a similar trend with a maximum at $x = 0.7$. Moreover, ^{57}Fe Mössbauer spectroscopy adequately explained the magnetic behaviour, the anisotropy constant, and saturation magnetization of low Co content samples. Finally, our study shows that the relaxation loss is a primary contributor to the SAR in $Co_xFe_{3-x}O_4$ NPs with low Co contents as well as their potential application in magnetic hyperthermia.

1. Introduction

Magnetic nanoparticles (MNPs) have triggered the attention of researchers in biomedical applications, such as magnetic resonance imaging, magnetic separation, drug delivery, bio-sensing, and as heat mediators in magnetic hyperthermia (MH) – an effective approach to eliminate cancer in conjunction with chemotherapy and radiation.[1–4] In MH application, the heating efficiency of MNPs under an ac magnetic field (ACMF), defined by the specific loss power (SLP) or the specific absorption rate (SAR), depends on many factors such as particle size (D), saturation magnetization (M_S), magneto-crystalline anisotropy constant (K), *etc.*[4–9]

The MNPs, including spinel ferrites, have been synthesized by various chemical methods such as co-precipitation,[9–12] hydrothermal,[13–16] thermal decomposition,[4–8,17,18] *etc.* Cation distribution, particle size, size distribution and consequently the magnetic properties and application of MNPs are influenced by the synthesis methods. It is well known that the thermal decomposition method provides better control over shape, crystal size, and size distribution of MNPs, as compared to the co-precipitation. However, the latter is widely used for the synthesis of MNPs for biomedical applications due to its simplicity and productivity.

For MH application, iron oxides (IONs) such as magnetite (Fe_3O_4) and maghemite (γ-Fe_2O_3) have been most investigated, owing to their appropriate magnetic properties, biocompatibility and cost-effectiveness. However, their relatively low heating efficiency hampers the practical MH application of the IONs. To overcome this challenge, various approaches have been taken to enhance the magnetic properties of the IONs through optimizing the particle size and shape (nanocubes, nanowire, *etc.*), composition and structure (multi-core, core/shell).[5–8] One of the possible approaches is to tailor the magnetic anisotropy of the IONs by varying the particle shape or morphology.[5,7] In this context, cobalt (Co) doped magnetite ($Co_xFe_{3-x}O_4$) NPs appear to be a promising candidate as $CoFe_2O_4$ possesses a large K ($>10^6$ erg cm^{-3}), which is one order of magnitude higher than that of Fe_3O_4 ($\sim10^4 \div 10^5$) erg cm^{-3}.[19]

[a]Institute of Materials Science, Vietnam Academy of Science and Technology, Hanoi, Vietnam. E-mail: manhdh.ims@gmail.com

[b]Graduate University of Science and Technology, Vietnam Academy of Science and Technology, Hanoi, Vietnam

[c]Duy Tan University, Da Nang, Viet Nam

[d]Institute of Low Temperatures and Structure Research, Polish Academy of Sciences, 50-422 Wroclaw, Poland

[e]Science and Technology Advances, Van Lang University, Ho Chi Minh city, Binh Thach, Vietnam

[f]Department of Physics and Oxide Research Center, Hankuk University of Foreign Studies, Yongin 17035, Republic of Korea

[g]Department of Physics, University of South Florida, Tampa, FL 33620, USA

† Electronic supplementary information (ESI) available. See DOI: 10.1039/d1ra07407e

A large body of work on the effect of Co content on the magnetic and heating properties of the $Co_xFe_{3-x}O_4$ NPs has been reported in the literature.[9,10,12,13,17,18,20] However, the results reported in those studies are either inconsistent or contradictory with each other, arising from the differences in the methods used for the samples' synthesis, as well as from how the magnetic and heating properties were characterized and analysed. For example, Yasemian et al.[10] claimed that the saturation magnetization (M_S) decreased with increase in the Co content. However, they could not confirm which site Co^{2+} ions occupied, because they did not perform Mössbauer studies. In contrast, Dutz et al.[12] reported that the M_S increased with Co content due to the gradual decrease of the maghemite phase (with lower values of bulk M_S compared magnetite and cobalt ferrites) for lower content and larger particle size for higher content, respectively. Their Mössbauer spectral analysis showed higher spin fluctuations for intermediate to high Co contents but did not provide a direct comparison with the M_S obtained from the magnetometry measurement. Li et al.[20] used Mössbauer spectroscopy to characterize the superparamagnetic properties of $Co_xFe_{3-x}O_4$ NPs for higher Co contents ($x = 0.4-1$) but not for lower ones.

In this work, we have performed a detailed study of the structural, magnetic and heating properties of $Co_xFe_{3-x}O_4$ NPs synthesized using a standard co-precipitation method. Our aim is to clarify effects of both Co content and particle size on the magnetic and heating properties of $Co_xFe_{3-x}O_4$ NPs. Apart from characterizing their morphological and structural properties, the magnetic properties of the NPs are comprehensively studied using DC magnetometer and Mössbauer spectroscopy. Finally, the hyperthermia properties are investigated, and the results (the SAR values) are discussed in relation to the magnetic properties of the NPs.

2. Experimental

2.1. Materials

Iron Chloride salts of Iron ($FeCl_3\cdot6H_2O$, 99% and $FeCl_2\cdot4H_2O$, 99%) and Co ($CoCl_2\cdot4H_2O$, 99%), sodium hydroxide (NaOH, 97%) were purchased from Merck (Germany). All materials were used as received. Distilled water was used in synthesizing the samples.

2.2. Synthesis

The co-precipitation synthesis of $Co_xFe_{3-x}O_4$ NPs with different composition procedures was as follows: the reagents, a definite stoichiometric proportion of iron chloride salts ($FeCl_3\cdot6H_2O$, $FeCl_2\cdot4H_2O$) and $CoCl_2\cdot4H_2O$ were mixed and dissolved in 50 mL of deionized water. The mixture was then heated to 80 °C in a water bath under stirring. Then, the aqueous of NaOH (2 M) was added quickly to the mixture until reaching a pH value of ~13. The heating continued while keeping the solution temperature at 80 °C for 30 min until forming a black precipitation, representing the desired magnetic phase. The black mixture was then cooled down to room temperature and separated by magnets. Finally, the precipitates were thoroughly washed with distilled water to eliminate chloride ions, and dried in an oven at 80 °C overnight. Accordingly, seven $Co_xFe_{3-x}O_4$ samples with different Co contents from $x = 0$ to 1 were labelled as S1–S7, respectively.

2.3. Structural characterization

The structural properties were characterized using a Bruker D8–ADVANCE diffractometer with CuKα ($\lambda = 0.154$ nm) radiation. The average crystallite size (D_{XRD}) was determined by Rietveld method using a commercial X'Pert HighScore Plus software.[21] The morphology and chemical composition were investigated using a Hitachi S-4800 field emission scanning electron microscope (FE-SEM) equipped with an energy-dispersive X-ray (EDX) spectrometer. The TEM images were collected under transmission electron (TE) mode. The nanoparticles were dispersed in hexane, dropped on a carbon-coated copper grid and left to dry for TEM observations. The mean particle size (D_{TEM}) was obtained by measuring the average diameter of about 100 particles using the images collected in from different parts of the grid.

2.4. Magnetic characterization

The magnetic properties were investigated using a vibrating sample magnetometer (VSM) in the temperature range of 177–500 K and magnetic fields up to 11 kOe. The temperature dependent zero field cooled and field cooled magnetizations, $M_{ZFC}(T)$ and $M_{FC}(T)$, are measured in a weak magnetic field ($H_{probe} = 300$ Oe).

^{57}Fe Mössbauer spectra of studied samples were measured in transmission geometry with a conventional constant-acceleration spectrometer (ELEKTRONIKA JADROWA-Kraków) of a high velocity resolution (4096 channels), using a ^{57}Co source in a Rh matrix of 1.85 GBq (50 mCi). The velocity scale was calibrated at room temperature using a standard α-Fe iron foil with a full width at half maximum (FWHM) of 0.22 mm s^{-1}. The isomer shift of the α-Fe foil is -0.108694 mm s^{-1} and the internal hyperfine magnetic field is 32.9759 T at 300 K. In our spectrometer, the krypton counter (ELEKTRONIKA JADROWA-Kraków) and Helium cryostat (Oxford Instruments 8T-Spectromag) are equipped with Mylar windows, so the background spectrum from the Mössbauer spectrometer is deprived of Fe impurities.

2.5. Magnetic hyperthermia

The magnetic hyperthermia parameters were evaluated by using a commercially available UHF-20A Module at a fixed frequency of 450 kHz and adjusted amplitudes from 150 to 300 Oe.

3. Results and discussion

3.1. Microstructure, composition and morphology

The phase composition and crystal structure of the samples were confirmed by XRD analysis. Fig. 1a shows the XRD patterns of the samples, in which the distinctive peaks possess positions corresponding to the cubic structure of the Fe or Co ferrites. The gradual shift towards the lower angle of the representative
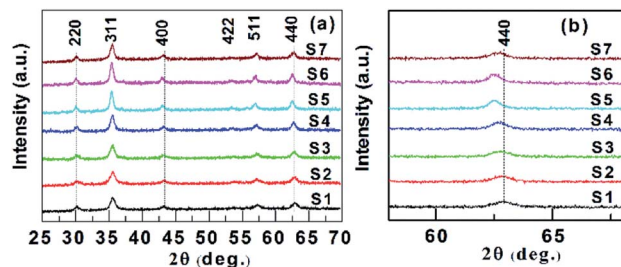
Fig. 1 (a) XRD patterns of $Co_xFe_{3-x}O_4$ ($x = 0-1$) nanoparticles. (b) Shift of the (440) reflection.

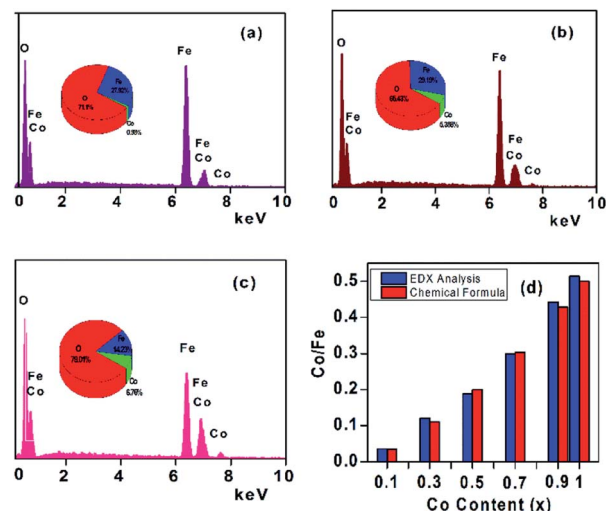**Fig. 2** EDX spectra of $Co_xFe_{3-x}O_4$ nanoparticles: (a) $x = 0.1$; (b) $x = 0.5$; and (c) $x = 1.0$. (d) Comparison of the Co/Fe atomic ratio obtained from the EDX analysis and the theoretical stoichiometry of all samples.

reflectance (440) (Fig. 1b), which is due to an increase of the interplane distances (d) in the spinel structure.[9] This result demonstrates the successful substitution of Co ions for Fe ions in the magnetite structure. However, it is also well known that the iron (magnetite and maghemite) and cobalt ferrite phases with similar structures cannot be distinguished by XRD alone.[22,23] The average crystallite sizes (D_{XRD}) were calculated from the width of the (220), (311), (400), (422), (511), and (440) lines, which are given in Table 1. The change of D_{XRD} (between 12.7 and 23.3 nm) with an increase of Co content was non-monotonic. Similar results have been reported for $Co_xFe_{3-x}O_4$ NPs by Gil *et al.*[11] Although the change of D_{XRD} with the increase of cobalt content is currently unclear, but Byrne *et al.*[24] suggested that the difference in the initial size of the ferrihydride NPs and/or the rate of Fe^{3+} ion reduction by reducing agents could cause the change of D_{XRD}.

The qualitative chemical composition was investigated by using EDX. Fig. 2a–c present typical EDX spectra for the samples with $x = 0$, 0.5, and 1 that confirmed the presence of Fe, Co, and O in the samples. The atomic ratios of Co/Fe obtained from the EDX analyses are in good agreement with the theoretical stoichiometry for all samples (Fig. 2d and Table 1). These results are almost similar to that reported by Yasemian *et al.*[10] for $Co_xFe_{3-x}O_4$ NPs ($x = 0-1$) obtained by the co-precipitation method.

Fig. 3 shows that the particles are in the nanometer range and roughly spherical in shape. The insets of these images show

Table 1 The structural properties of $Co_xFe_{3-x}O_4$ ($x = 0-1$) nanoparticles: Co (theoretically and experimental) content, average crystallite size (D_{XRD}) and particle size (D_{TEM})

Sample name	Co content (x)		D_{XRD} (nm)	D_{TEM} (nm)
	Theo.	Exp.		
S1	0	0	14.3	14.6
S2	0.1	0.08	12.7	13.5
S3	0.3	0.29	15.3	16.2
S4	0.5	0.48	18.6	20.8
S5	0.7	0.69	23.3	24.9
S6	0.9	0.85	22.9	23.8
S7	1	0.95	17.6	19.4

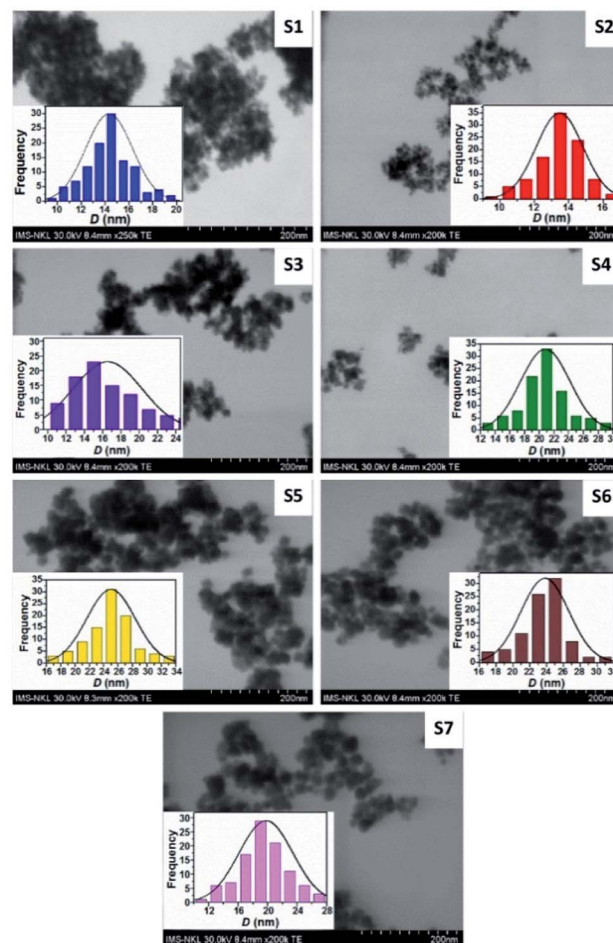**Fig. 3** TEM images of $Co_xFe_{3-x}O_4$ nanoparticles with different Co contents. Insets show the particle size distribution.

log-normal distributed nanoparticles. The D_{TEM} of samples exhibits good agreement with D_{XRD} obtained from the XRD data (Table 1). Therefore, grain size (D) will be used instead of crystal and/or particle size in the following heating and magnetic analysis and discussion.

3.2. Magnetic properties

Fig. 4(a) Presents typical $M_{ZFC}(T)$ and $M_{FC}(T)$ curves of three $Co_xFe_{3-x}O_4$ ($x = 0$, 0.1 and 0.3) samples showing an irreversible behavior below the peak temperature, identified by the maximum in the $M_{ZFC}(T)$ curve, corresponding the average blocking temperature (T_B) where the thermal energy is equivalent to the activation energy.[17,25]

A transition occurs from the ferromagnetic, FM, ($T < T_B$) to the superparamagnetic, SPM, ($T > T_B$) state. Thus, the magnetic behavior of S1 at 300 K is SPM, while the remaining samples are primarily FM. The T_B values of all samples are reported in Table 2. It is evident that the T_B shifts to a higher temperature with an increase in the Co content until $x = 0.7$ that may be due to the increased contribution of magnetocrystalline anisotropy of the NPs.[17] The T_B value decreased from $x = 0.7$ to $x = 1$, indicating that the magnetocrystalline anisotropy of NPs did not increase with increasing Co content. This result is consistent with previous reports, where the magnetocrystalline anisotropy in $Co_xFe_{3-x}O_4$ NPs decreased with increasing Co content from 0.75 to 1.[17,26]

The magnetic hysteresis loops (M–H) at 300 K for $Co_xFe_{3-x}O_4$ ($x = 0-1$) NPs are shown in Fig. 4(b). The M_S and coercivity (H_C) as functions of Co content extracted from the M–H loops are given in Table 2 and their trends are also shown in Fig. 5. The M_S increased from 54.4 emu g^{-1} to 71.1 emu g^{-1} with an increase of Co content (x) from 0 to 0.7, and decreased to 57.4 emu g^{-1} with a further increase of Co content (x from 0.7 to 1). Most of the reports on $Co_xFe_{3-x}O_4$ NPs synthesized by different methods[9,10,12,13,18,20] found the non-monotonic change of D with an increase of Co content, so their M_S was analyzed according to D. In our study, the increase of M_S with D was assumed by the reduced contribution of the surface effects (spin disorder behavior and/or magnetic dead layer).[9,25]

In contrast, Das *et al.*[17] found that the M_S values of Co_x-$Fe_{3-x}O_4$ NPs of the similar size remained almost unchanged with increasing Co content. The H_C and remanence

Table 2 Saturation magnetization (M_S), coercivity (H_C), blocking temperature (T_B), anisotropy constant (K), and specific absorption rate (SAR)

Sample name	M_S (emu g^{-1})	H_C (Oe)	T_B (K)	K (erg g^{-1})	SAR (W g^{-1})
S1	54.4	3	250	163	363.7
S2	53.4	32	310	1709	296.8
S3	55.6	232	425	12 899	234.1
S4	61.1	445	446	27 189	183.9
S5	71.1	770	516	54 747	163.0
S6	70.4	633	491	44 563	179.7
S7	57.4	318	401	18 253	196.5

magnetization (M_r) values reconfirm the superparamagnetic and ferromagnetic behavior for S1 and (S2, S3), obtained from the above $M(T)$ analysis. The trend of H_C with an increase of Co content as well D is similar to that of M_S (Fig. 5b). The change of H_C is related to the change of magnetic anisotropy, size of single domain NPs, *etc.*[9,17,18,27]

It is generally expected that the major substitution of Co^{2+} ions for Fe^{2+} ions in the spinel structure of magnetite nanoparticles leads to an increase in magnetic anisotropy.[9,10,17]

The anisotropy constant (K) can be simply estimated as follows:[10]

$$K = \frac{H_C M_S}{0.96} \quad (1)$$

The obtained K values are presented in Table 2. The variation behavior of K is similar to that of H_C and M_S. An increase in magnetic anisotropy with Co content is assumed due to the increasing number of octahedral sites occupied by Co ions and stronger LS coupling.[26,28] Oppositely, the decrease in magnetic anisotropy with further increasing of Co content may be due to the increased number of tetrahedral sites occupied by Co

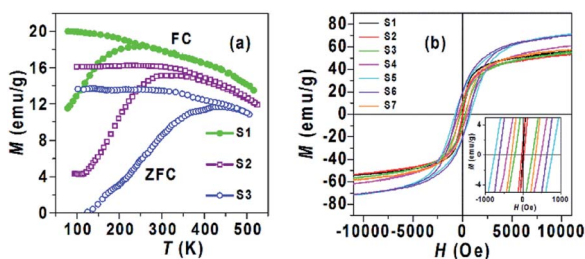**Fig. 4** (a) Zero-field-cooling (ZFC) and field-cooling (FC) magnetization curves of three typical samples S1, S2 and S3; (b) M–H loops of $Co_xFe_{3-x}O_4$ ($0 \le x \le 1$) samples. Inset shows the low field region of the M–H loops.
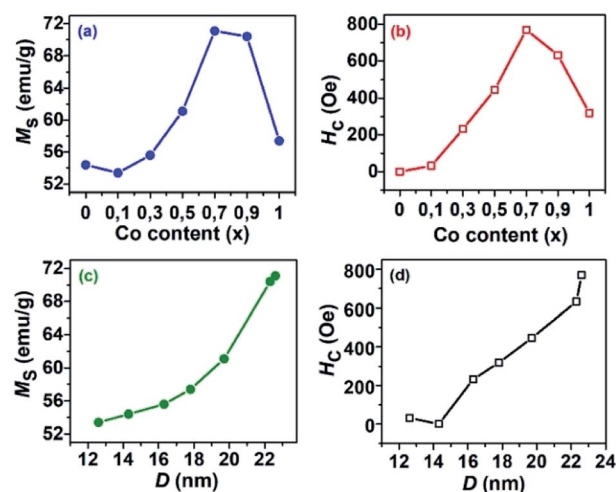

Fig. 5 Variation of saturation magnetization (M_S) and coercivity (H_C) as functions of (a and b) cobalt content in $Co_xFe_{3-x}O_4$ ($0 \le x \le 1$) nanoparticles and (c and d) particle size.

ions.[20,29] Besides, there are several factors such as size, shape, surface, *etc.*17 that can contribute to magnetic anisotropy.

The difference between K values of samples (S4 and S7) or (S5 and S6) indicates that the effect of D on magnetic anisotropy should be accounted for magnetic anisotropy. Overall, our experiments showed that the magnetic behaviour of $Co_xFe_{3-x}O_4$ NPs at 300 K is superparamagnetic for the S1 and ferromagnetic for the remaining samples. In addition, the saturation magnetization, the coercivity, the anisotropy constant, and the blocking temperature followed a similar trend with an increase of Co content.

In obtain complementary information about the magnetic property of $Co_xFe_{3-x}O_4$ ($x = 0$, 0.1 and 0.3) NPs, we performed measurements of ^{57}Fe Mössbauer spectroscopy at 300 K. Before starting discussion on the experimental ^{57}Fe Mössbauer data, it is important to highlight some results from previous reports. First of all, the bulk Fe_3O_4 sample has an inverse spinel structure, in which half of the Fe^{3+} ions occupy the 8a tetrahedral site (denoted as A sites) and the remaining Fe atoms with equal quantities of Fe^{3+} and Fe^{2+} ions are located on 16c octahedral (B sites) positions.[33,34] Therefore, from the theoretical point of view, the Mössbauer spectra should be comprised of two sextet lines corresponding to the respective A and B sites of the Fe ions. Such a behaviour was well documented, *e.g.*, by Topøse *et al.*[30] However, since the particle sizes of our samples lie in the range of 12.7 and 15.3 nm, we should refer our data also to those obtained on ferrite nanoparticles.[20,24,30–32,35]

Li *et al.*[20] showed Mössbauer spectra of $Co_xFe_{3-x}O_4$ NPs ($x = 0.4$, 0.6, 0.8 and 1.0) consisting of the central doublet superposed on sextet pattern. The presence of the doublet was interpreted as due to superparamagnetic properties of nanoparticles. Apparently, the Mössbauer spectrum of S1 in Fig. 6 for Fe_3O_4 NPs bears a resemblance to that of the 18 nm-sized Fe_3O_4 particles reported by Topøse *et al.*[30] and to that of the 11.8 nm-sized Fe_3O_4 particles reported by McNab.[31] The observed feature implies that the Fe_3O_4 NPs are in the superparamagnetic regime. Taking into account the presence of the super-paramagnetic doublet and two sextets coming from the sites A and B, *i.e.*, A-Fe^{3+} and B-(Fe^{3+}–Fe^{2+}), we have fitted a model to the data, and obtained an acceptable convergence. Using the same model, we have attempted to analyze the data of S2 ($x = 0.1$) and S3 ($x = 0.3$). Unfortunately, the results of the fits were not satisfying enough. Because the substituting Co atoms can get into the A, B or both sites, we propose to consider not two but auxiliary five sextets. Two sextets come from sites A and B, *i.e.*, A-Fe^{3+} and B-(Fe^{3+}–Fe^{2+}), the three remaining sextets simply as an issue from electron hopping due to the Co-substitution, *i.e.*, A-(Fe^{3+}–Co^{2+}), B-(Fe^{3+}–Co^{2+}) and B-(Fe^{2+}–Co^{2+}). Such a situation could appear if allowing for the two-level model developed by Blume and Tjon,[36] where the magnetic hyperfine field fluctuates between ± 55 T and quadrupole shift of 0.1 mm s^{-1}. In the case of relaxation times below 1 ns, the Mössbauer spectra should consist of paramagnetic lines. Otherwise, there occur clear sextets. Obviously, in the situation between two limits, the Mössbauer lines should be broadened and may be composed of sextets and doublet. In the studied samples, the distribution of particle sizes is around 12.7 nm in S2 and 15.3 nm in S3,
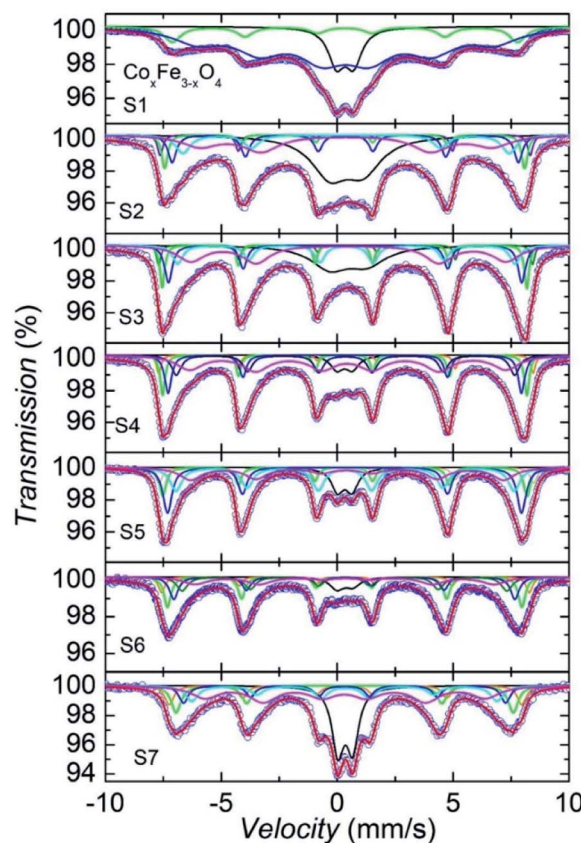

Fig. 6 Mössbauer spectra of $Co_xFe_{3-x}O_4$ NPs at 300 K. One super-paramagnetic doublet and two sextets respective for the A and B sites were taken into consideration for Fe_3O_4 NPs (S1) and a superposition of one short-time relaxation doublet and five sextets for the remaining samples (S2–S7).

resulting in a distribution of relaxation times of the NPs in these samples. Usually, the fraction of smaller particles has shorter relaxation times, urging a doublet component.

Allowing such six components in the spectra analysis has yielded very good convergence of the fit. The detailed description of fitting spectra for each sample is depicted as Fig. SF3–SF8,† and the concise description of the fitting spectra is shown as solid lines in Fig. 6. We ascribe the black line (circle in Fig. 7) to the doublet, the violet and green lines (triangles in Fig. 7) to tetragonal respective A-(Fe^{3+}–Co^{2+}) and A-Fe^{3+} sextets, while the blue, cyan and magenta colors (diamond, star and pentagon, respectively, in Fig. 7) conform to B-(Fe^{3+}–Fe^{2+}), B-(Fe^{3+}–Co^{2+}) and B-(Fe^{2+}–Co^{2+}) sextets, respectively. As a general remark, it must be underlined that while previous studies, *e.g.*,[30,31] showed the similar Mössbauer spectra, the authors did not attempt to analyze their data in detail. Therefore, the model proposed by us here represents the first effort, which should be verified in future investigations.

We should also remark the line widths, which can be easily distinguished one from the other. It is clear that the line width in sextet of B-sites (blue color in S1, and magenta in the remaining compositions) is decisively largest. There are at least two reasons causing broadening of the Mössbauer lines: (i) the
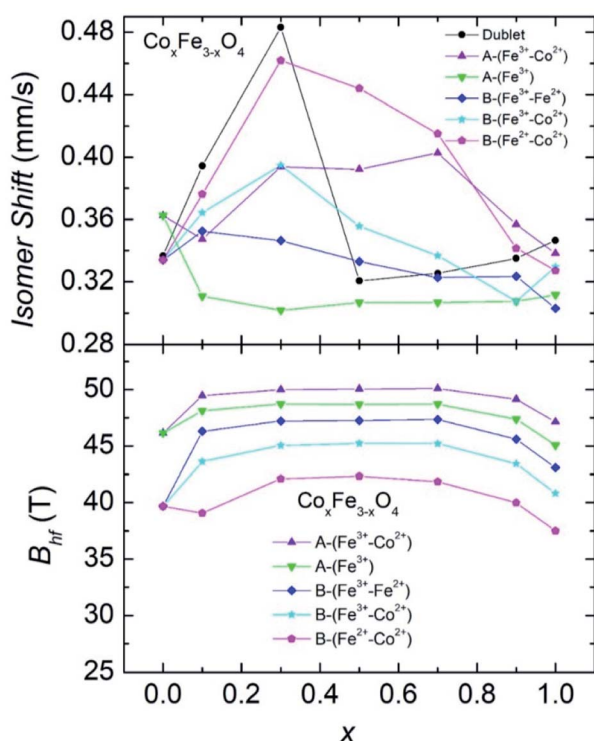
Fig. 7 Isomer shifts δ and hyperfine fields B_{hf} in $Co_xFe_{3-x}O_4$ NPs at 300 K as a function of Co content x.

mean lifetime of the excited states, δ, and (ii) the mean square displacement $\langle x^2 \rangle$. The first reason related to the period of the excitation between the ground and excited states impinges the Lorentzian function, $I(E) = \dfrac{\left(\dfrac{\Gamma}{2}\right)^2}{(E - E_0)^2 + (\Gamma/2)^2}$ of the resonant ^{57}Fe atom, while mean square displacement $\langle x^2 \rangle$, involves both lattice vibrations and collective motions affects the recoil-free fraction, $f = \exp - \{\dfrac{(2\pi)^2 \langle x \rangle^2}{\lambda^2}\}$, where λ is the wave length of γ-radiation. We presume that the relaxation process and charge hopping happen between different types of ions is the main reason behind the broadened Mössbauer lines and to assign these lines to the magnetically blocked fraction of the spectra.

We should emphasize that the difference in shape of doublet between S1 and S2/S3, the symmetric doublet in S1 may indicate the superparamagnetic behaviour, whereas asymmetric doublet in S2 and S3, arises from the various relaxation times of size-particle fractions, bring out a combined behaviour of short-relaxation time doublet and magnetic sextets. It is worth recalling that similar asymmetric doublet in the previous report by Li *et al.*[20] was untangled in terms of the super-paramagnetism. From the fit of the Mössbauer spectra, we have obtained several hyperfine parameter values, including of isomer shift (δ), full width at half maximum (FWHM), quadrupole splitting (ΔE), intensity ratio $A12$, hyperfine field (B_{hf}) and population (I), which are summarized in Table 3. Plot of the

isomer shift and hyperfine field *vs.* Co contents is displayed in Fig. 7.

It can be seen from Fig. 7 that the smooth and continuous changes are observed in the plot of $B_{hf}(x)$, whereas distinctive features at different sub-spectra in the $\delta(x)$ dependences emerge. Nevertheless, one finds a consistent explanation for the $\delta(x)$ behavior. Let us recall the equation for isomer shift of an absorber with respect to source:

$$\delta = \frac{2}{5}Ze^2\left(R_{ex}^2 - R_{gs}^2\right)\left|\rho(0)_A - \rho(0)_S\right|, \quad (2)$$

where Z is the nuclear charge, R_{ex} and R_{gs} are the nuclear charge radii in the excited and ground states, respectively, and $\rho(0) = -e|\Psi(0)|^2$ is the electron charge density at the resonant nucleus in the absorber (A) and source (S). For ^{57}Fe Mössbauer spectroscopy, the difference between the radius of the isomeric excited state and that of the ground state is negative. The increase of δ observed in the spectrum of A-(Fe^{3+}–Co^{2+}) and B-(Fe^{2+}–Co^{2+}) indicates a decrease in the s-electron density, being an effect of a raise in the d-type electron density. Usually, the 3d electrons partly screen the nuclear charge from the 4 s electrons, so during the substituting of Co atoms the compound gains one more electron, which gives rise to better shielding and in a consequence reduces the s-electron density. The isomer shift δ is a two-component contribution, the chemical isomer shift δ_C and Mössbauer second-Doppler shift, δ_{SOD}. The decrease in $\delta(x)$ for $x > 0.3$ is probably owing to the change of the second to the mean square velocity $\langle v^2 \rangle$, involved in $\delta_{SOD} = -\langle v^2 \rangle/c^2$, where c is the velocity of light, because $\langle v^2 \rangle$ is affected by lattice dynamics.

The change in δ values of the spectrum of B-(Fe^{3+}–Fe^{2+}) and A-(Fe^{3+}) with increasing concentration x from $x = 0.7$ may suggest a lessening concentration of the Fe^{3+}/Fe^{2+} due to the Co-substitution. An inspection of δ values between sub-spectra implies that the substitution of Fe by Co reluctantly occupies the B-(Fe^{3+}–Co^{2+}) site, but rather preferentially takes place in the B-(Fe^{2+}–Co^{2+}) and A-(Fe^{3+}–Co^{2+}) sites. To be precise, based on the eqn (3), we may estimate the Co-content occupying positions A and B upon the substitution. At the concentration $x = 0.3$, we expect that the substituting Co atoms locate at the 8a position up to 32%, at the 16c (Fe^{2+}–Co^{2+}) up to 49% and at the 16c (Fe^{3+}–Co^{2+}) up to 16%.

A comparison of the FWHM values reveals remarkable connection between FWHM of sub-spectra. The FWHM values of dublet and B-(Fe^{2+}–Co^{2+}) subspectrum are always larger than those of the remaining. This observation suggests that the behaviour results from a relaxation dynamic, or charge/electron hopping on the octahedral sites between the Fe^{3+} and Fe^{2+} ions.

A detailed analysis of the hyperfine field values ordinarily enables the estimation of change in the magnetic moments of Fe moments across the x contents. Interestingly, B_{hf} was found to increase with Co content in $Co_xFe_{3-x}O_4$ NPs up to $x = 0.5$, and then from $x = 0.7$ B_{hf} clearly drag down. This finding agrees well with the concentration dependence of the saturation magnetization (see Fig. 5a).

However, it is difficult to find out a direct relation between B_{hf} values and magnetic moments of Fe, like in the situation of

Table 3 Hyperfine parameters for $Co_xFe_{3-x}O_4$ NPs at 300 K. The fitted values of isomer shift δ (mm s^{-1}), full width at half maximum FWHM (mm s^{-1}), intensity ratio A12, quadrupole splitting ΔE (mm s^{-1}), hyperfine field B_{hf} (T) and population (I) for respective sub-spectra

Sample name	Sub-spectra	δ (mm s^{-1})	FWHM (mm s^{-1})	A12	ΔE (mm s^{-1})	B_{hf} (T)	I (%)
	Doublet	0.3367	0.8599	0.9389	0.7411	0	14.17
S1	A-Fe^{3+}	0.3340	0.8736	2.047	0.0009	46.15	12.92
	B-(Fe^{3+}–Fe^{2+})	0.3625	2.456	1.956	0.0020	39.68	72.91
	Doublet	0.3944	1.9197	0.5308	1.4498	0	34.08
	A-(Fe^{3+}–Co^{2+})	0.3473	0.2716	1.2835	−0.008	49.46	5.47
	A-Fe^{3+}	0.3109	0.3040	2.7461	0.0155	48.13	8.15
S2	B-(Fe^{3+}–Fe^{2+})	0.3525	0.4355	1.2658	−0.012	46.30	14.31
	B-(Fe^{3+}–Co^{2+})	0.3784	0.7620	1.3939	0.0056	43.63	12.04
	B-(Fe^{2+}–Co^{2+})	0.3763	1.8978	0.6981	0.0101	39.08	25.95
	Doublet	0.4832	1.9885	0.5569	1.5936	0	23.52
	A-(Fe^{3+}–Co^{2+})	0.3938	0.2227	1.3567	−0.0654	49.99	5.56
	A-Fe^{3+}	0.3019	0.2401	2.0557	0.0225	48.72	12.25
S3	B-(Fe^{3+}–Fe^{2+})	0.3464	0.3917	1.6024	−0.0149	47.22	14.38
	B-(Fe^{3+}–Co^{2+})	0.3947	0.5275	1.2813	−0.0040	45.05	16.03
	B-(Fe^{2+}–Co^{2+})	0.4619	1.4264	0.9014	0.0372	42.11	28.26
	Doublet	0.3206	0.6592	0.5042	0.6605	0	6.47
	A-(Fe^{3+}–Co^{2+})	0.3922	0.2313	1.3284	−0.040	50.05	6.15
S4	A-Fe^{3+}	0.3069	0.2427	1.9145	0.0277	48.69	13.52
	B-(Fe^{3+}–Fe^{2+})	0.3330	0.3422	1.7244	−0.016	47.26	14.74
	B-(Fe^{3+}–Co^{2+})	0.3557	0.4930	1.2233	0.0023	45.24	18.70
	B-(Fe^{2+}–Co^{2+})	0.4439	1.3566	0.9227	0.0267	42.33	40.41
	Doublet	0.3254	0.6361	0.5059	0.6284	0	9.26
	A-(Fe^{3+}–Co^{2+})	0.4027	0.3609	1.3075	−0.0243	50.09	8.32
S5	A-Fe^{3+}	0.3069	0.3296	1.6581	0.0495	48.72	13.10
	B-(Fe^{3+}–Fe^{2+})	0.3227	0.4635	1.7180	−0.0166	47.34	21.73
	B-(Fe^{3+}–Co^{2+})	0.3368	0.6075	1.1624	0.0035	45.21	26.38
	B-(Fe^{2+}–Co^{2+})	0.4151	1.1255	1.1114	0.0208	41.85	21.19
	Doublet	0.3350	0.7452	0.5664	0.6893	0	7.73
	A-(Fe^{3+}–Co^{2+})	0.3568	0.3300	1.7885	−0.0057	49.15	10.32
S6	A-Fe^{3+}	0.3077	0.3562	1.3862	0.0259	47.38	22.46
	B-(Fe^{3+}–Fe^{2+})	0.3234	0.4405	1.6998	−0.0354	45.61	19.64
	B-(Fe^{3+}–Co^{2+})	0.3077	0.5567	1.1332	0.0140	43.43	19.45
	B-(Fe^{2+}–Co^{2+})	0.3415	1.2473	1.0122	−0.0581	39.99	20.39
	Doublet	0.3465	0.6155	0.5129	0.6390	0	21.25
	A-(Fe^{3+}–Co^{2+})	0.3382	0.4639	1.5581	0.0330	47.14	10.49
	A-Fe^{3+}	0.3118	0.5094	1.5179	0.0158	45.08	12.85
S7	B-(Fe^{3+}–Fe^{2+})	0.3032	0.4870	1.5099	0.0266	43.08	10.93
	B-(Fe^{3+}-Co^{2+})	0.3295	0.6831	1.7316	−0.038	40.83	14.19
	B-(Fe^{2+}–Co^{2+})	0.3272	1.4377	0.7696	0.0324	37.51	30.27

solid compounds where the ratio $B_{hf}/\mu_{Fe} = 33.9$ T/2.2 μ_B can usually be used as the first approximation for scaling. The difficulties in the interpretation appear here due to different sizes of nanoparticles in the studies materials. There exist at least two physical phenomena, which may provide a misinterpretation, associated with superparamagnetic properties and dynamic relaxations of small size nanoparticles. This issue will be investigated further from a quantitative point of view, based on the DFT calculations.

In addition to the discussion above, we may contemplate on the concentration dependence of the first-to-second area ratio $A12$. Because, the quantity $A12$ determines by the canting angle θ between the magnetization vector and the easy axis, we are able to estimate θ, using the following equations: For sextets, $A_1(\theta) = 3(1 + \cos^2 \theta)/16$, $A_2(\theta) = 4(1 - \cos^2 \theta)/16$ and for doublet $A_{3/2}(\theta) = 3(1 + \cos^2 \theta)/8$ and $A_{1/2}(\theta) = 3(5/3 - \cos^2 \theta)/8$. The calculated values $A12$ for a sextet of the position A(Fe^{3+}–Co^{2+})

and B(Fe^{2+}–Co^{2+}) show the canting angle θ at the A position rapidly increases from 47° in $x = 0$ to 58° in $x = 0.1$. With increasing x, the angle θ levels off till $x = 0.7$, and then drag down with further increasing x. Synchronously, the change in θ at the position B(Fe^{3+}–Fe^{2+}) resembles the concentration behaviour of the saturation magnetization and absorption rate (see below). Thus, the magnitude of the canting angle may correlate with the changes in the magnetic quantities.

3.3. Magnetic hyperthermia properties

In order to evaluate the effect of Co content on the heating efficiency (*i.e.*, the specific absorption rate, SAR), the Co$_x$-Fe$_{3-x}$O$_4$ NPs were dispersed in water with a nanoparticle content of 1 mg mL^{-1} for each measurement and exposed to an AC magnetic field. The temperature measurements as a function of the time were performed under non-adiabatic conditions.
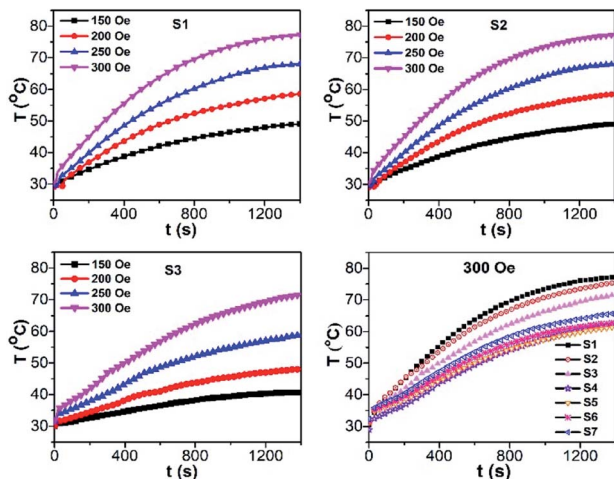
Fig. 8   Field exposure time dependence of temperature growth in an ACMF with adjusted amplitudes (150 to 300 Oe) and frequency (450 kHz) of $Co_xFe_{3-x}O_4$ suspended samples with different Co contents.

Fig. 8 shows the exposure time dependence of the temperature (T vs. t) curves in the ACMF with adjusted amplitudes of 150–300 Oe and a fixed frequency of 450 kHz. The samples S1, S2, and S3 with low Co content and similar M_S, K, the saturation heating temperature (T_S), which extracted from the T vs. t curves, increased with the field amplitude. For all samples investigated, the obtained T_S in a field of 300 Oe and 450 kHz decreased with increasing Co content until $x = 0.7$ and then slightly increased with further increase in Co content. The samples with low Co content ($x = 0$ and 0.1), a field amplitude of 150 Oe is sufficient to obtain T_S in the range 40–44 °C, where tumor cells can be destroyed. These results showed that these samples have potential applications in magnetic hyperthermia therapy.

The heating efficiency (SAR) of the nanoparticles can be evaluated by using the following equation:[4]

$$SAR = C_p \frac{\Delta T}{\Delta t} \frac{m_s}{m_n}, \qquad (3)$$

where C_p is the specific heat of the solution, m_s the mass of the solution, m_n the mass of the nanoparticles, and $\Delta T / \Delta t$ is the initial slope of the heating curve.

The SAR values of all the samples at ACMF of 300 Oe and 450 kHz are presented in Fig. 9a and Table 2. The trend of SAR with change of Co content is opposite to that of M_S or H_C. The SAR decreased with increasing Co content, which reflects the contribution of heat generation mechanisms under ACMF such as the relaxation (Néel and Brown) and hysteresis losses. The first is usually dominant in superparamagnetic NPs, while the second is in single-domain ferromagnetic NPs (see ref. 35 for more details). The contribution of each mechanism to the SAR depends on many parameters, such as D, M_S, H_C, K, etc.[37]

For superparamagnetic NPs, the experimental results and predictions based on linear response theory have shown that the SAR is directly proportional to M_S and peaks at a certain value of K, but both parameters M_S and K are also changed with D.[9,13,35] Therefore, a maximum SAR value can be obtained with a certain D and K. In fact, the highest SAR has obtained with D of 14.3 nm and K of 163 erg g^{-1} for S1 in this study (as shown in Table 2). For single-domain ferromagnetic NPs, under a fixed amplitude (H) the hysteresis loss peaks at a certain value of H_C and then it will decrease with a higher value of H_C because the H is insufficient to reverse the magnetization completely. Experimental reports have shown such H_C values to be around $0.4H$.[10,12] In practice, the highest SAR value was obtained for superparamagnetic NPs (S1). The other authors also observed a similar trend for $Co_xFe_{3-x}O_4$ ($0 \leq x \leq 1$) ferromagnetic NPs.[9,13] These results convey that in the $Co_xFe_{3-x}O_4$ ($x = 0$–1) NPs, the relaxation loss contributes more dominantly to the SAR as compared to the hysteresis loss.

The field amplitude dependences of SAR for S1, S2, and S3 at a fixed frequency of 450 kHz are presented in Fig. 9b. It can be seen that the SAR depends on the square of the field amplitude between 150 Oe and 300 Oe for these samples, even though their coercivities are different. Such dependence has been reported for nanoparticles in the superparamagnetic regime, where heat generation is mainly resulted from the contribution of the relaxation loss.[38–40]

4.   Conclusion

We have performed a systematic study of the effect of cobalt content on the structural, magnetic and hyperthermia properties of $Co_xFe_{3-x}O_4$ ($0 \leq x \leq 1$) nanoparticles. The XRD and TEM analyses confirmed the formation of spherical nanoparticles with similar crystal and particle sizes for each Co content. Magnetic measurements on $Co_xFe_{3-x}O_4$ ($0 \leq x \leq 1$) nanoparticles indicated that their magnetic parameters (saturation magnetization, coercivity, anisotropy constant, and blocking temperature) followed a similar trend with a maximum at $x = 0.7$. The analysis of the Mössbauer spectra reveals that the substitution of Co for Fe preferentially takes place in the A-(Fe^{3+}–Co^{2+}) and B-(Fe^{2+}–Co^{2+}) sites, but the B-(Fe^{3+}–Co^{2+}) site. In consistency with the magnetization data, the Mössbauer study also confirms the superparamagnetic nature of S1 (the undoped sample, Fe_3O_4) but the ferromagnetic characteristic of the remaining Co-doped samples at room temperature. The issue of Mössbauer spectroscopy of non-uniform sized samples should be to encourage further investigations, especially regarding the
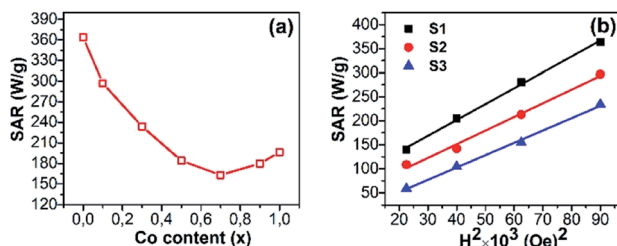

Fig. 9   Specific absorption rate (SAR) as a function of (a) the Co content measured at a fixed frequency of 450 kHz and 300 Oe for all samples and (b) the field amplitude for 3 samples.

low-temperature properties and the evolutionary relationships between our studies of $Co_xFe_{3-x}O_4$ for $x = 0–1$ and the previous study for $x = 0.4–1.0$.[20] Our hyperthermia study has revealed that the magnetic characteristics and SAR exhibit an opposite trend with an increase of the Co content in nanoparticles. Moreover, the minor contribution of the hysteresis loss to the SAR in the NPs with strong magnetic anisotropy, whose coercivity is comparable to the amplitude of the ACMF, was also reconfirmed. This study also shows that $Co_xFe_{3-x}O_4$ ($x = 0$ and 0.1) nanoparticles are suitable candidate materials for magnetic hyperthermia therapy.

Author contributions

L. T. H. Phong, T. N. Bach, D. K. Tung synthesized all the nanoparticles (except 7 nm spheres), carried out their structural analysis (SEM) and wrote the Synthesis section. P. H. Nam, B. X. Khuyen, B. S. Tung performed magnetic and some of colorimetric hyperthermia measurements (ZFC/FC and M–H loops). V. D. Lam, N. X. Phuc, The-Long Phan contributed to the analysis and the evaluation of the results. Thi Ly Mai makes some modifications to Fig. 6 and 7 and also to Table 3. D. H. Manh, T. V. Hung, and Manh Huong Phan coordinated and managed the experimental methods and assisted in the interpretation of the results, and guided the overall preparation of the paper.

Conflicts of interest

The authors declare no competing financial interest.

Acknowledgements

References

1 K. Maier-Hauff, F. Ulrich, D. Nestler, H. Niehoff, P. Wust, B. Thiesen, H. Orawa, V. Budach and A. Jordan, Efficacy and safety of intratumoral thermotherapy using magnetic iron-oxide nanoparticles combined with external beam radiotherapy on patients with recurrent glioblastoma multiforme, *J. Neurooncol.*, 2011, **103**, 317–324, DOI: 10.1007/s11060-010-0389-0.

2 S. V. Spirou, M. Basini, A. Lascialfari, C. Sangregorio and C. Innocenti, Magnetic Hyperthermia and Radiation Therapy: Radiobiological Principles and Current Practice, *Nanomaterials*, 2018, **8**, 410, DOI: 10.3390/nano8060401.

3 Z. Hedayatnasab, F. Abnisa and W. M. A. W. Daud, Review on magnetic nanoparticles for magnetic nanofluid hyperthermia application, *Mater. Des.*, 2017, **123**, 174–196, DOI: 10.1016/J.MATDES.2017.03.036.

4 T. H. P. Le, H. M. Do, H. N. Pham, T. P. Pham, J. Kováč, I. Skorvanek, T. L. Phan, M.-H. Phan and X. P. Nguyen, High heating efficiency of interactive cobalt ferrite nanoparticles, *Adv. Nat. Sci.: Nanosci. Nanotechnol.*, 2020, **11**, 045005, DOI: 10.1088/2043-6254/abbc68.

5 Z. Nemati, J. Alonso, I. Rodrigo, R. Das, E. Garaio, J. Á. García, I. Orue, M.-H. Phan and H. Srikanth, Improving the Heating Efficiency of Iron Oxide Nanoparticles by Tuning Their Shape and Size, *J. Phys. Chem. C*, 2018, **122**, 2367–2381, DOI: 10.1021/acs.jpcc.7b10528.

6 S. Tong, C. A. Quinto, L. Zhang, P. Mohindra and G. Bao, Size-Dependent Heating of Magnetic Iron Oxide Nanoparticles, *ACS Nano*, 2017, **11**, 6808–6816, DOI: 10.1021/acsnano.7b01762.

7 R. Das, J. Alonso, Z. N. Porshokouh, V. Kalappattil, D. Torres, M.-H. Phan, E. Garaio, J. Á. García, J. L. S. Llamazares and H. Srikanth, Tunable High Aspect Ratio Iron Oxide Nanorods for Enhanced Hyperthermia, *J. Phys. Chem. C*, 2016, **120**, 10086–10093, DOI: 10.1021/acs.jpcc.6b02006.

8 J. H. Lee, J. T. Jang, H. S. Choi, S. H. Moon, S. H. Noh, J. W. Kim, J. G. Kim, I. I. S. Kim, K. I. Park and J. Cheon, Exchange-coupled magnetic nanoparticles for efficient heat induction, *Nat. Nanotechnol.*, 2011, **6**, 418–422, DOI: 10.1038/nnano.2011.95.

9 H. Jalili, B. Aslibeiki, A. G. Varzaneh and V. A. Chernenko, The effect of magneto-crystalline anisotropy on the properties of hard and soft magnetic ferrite nanoparticles, *Beilstein J. Nanotechnol.*, 2019, **10**, 1348–1359, DOI: 10.3762/bjnano.10.133.

10 A. R. Yasemian, M. A. Kashi and A. Ramazani, Exploring the effect of Co content on magnetic hyperthermia properties of $Co_xFe_{3-x}O_4$ nanoparticles, *Mater. Res. Express*, 2020, **7**, 016113, DOI: 10.1088/2053-1591/ab6a51.

11 A. F. Gil, O. Benavides, S. M. Vargas, L. D. L. C. May and C. P. Carachure, *Int. J. Metall. Met. Phys.*, 2020, **5**, 047, DOI: 10.35840/2631-5076/9247.

12 S. Dutz, N. Buske, J. Landers, C. Gräfe, H. Wende and J. H. Clement, Biocompatible Magnetic Fluids of Co-Doped Iron Oxide Nanoparticles with Tunable Magnetic Properties, *Nanomaterials*, 2020, **10**, 1019, DOI: 10.3390/nano10061019.

13 Z. E. Gahrouei, S. Labbaf and A. Kermanpur, Exploring the effect of Co content on magnetic hyperthermia properties of $Co_xFe_{3-x}O_4$ nanoparticles, *Phys. E*, 2019, **116**, 113759, DOI: 10.1016/j.physe.2019.113759.

14 T. Sodaee, A. Ghasemi and R. S. Razavi, Cation distribution and microwave absorptive behavior of gadolinium substituted cobalt ferrite ceramics, *J. Alloys Compd.*, 2017, **706**, 133–146, DOI: 10.1016/j.jallcom.2017.02.233.

15 K. V. Chandekar and K. M. Kant, Estimation of the spin–spin relaxation time of surfactant coated $CoFe_2O_4$ nanoparticles by electron paramagnetic resonance spectroscopy, *Phys. E*, 2018, **104**, 192–205, DOI: 10.1016/j.physe.2018.06.016.

16 S. Singh and N. Khare, Defects/strain influenced magnetic properties and inverse of surface spin canting effect in

single domain $CoFe_2O_4$ nanoparticles, *Appl. Surf. Sci.*, 2016, **364**, 783, DOI: 10.1016/j.apsusc.2015.12.205.

17 R. Das, N. P. Kim, S. B. Attanayake, M.-H. Phan and H. Srikanth, Role of Magnetic Anisotropy on the Hyperthermia Efficiency in Spherical $Fe_{3-x}Co_xO_4$ ($x = 0-1$) Nanoparticles, *Appl. Sci.*, 2021, **11**, 930, DOI: 10.3390/app11030930.

18 A. Sathya, P. Guardia, R. Brescia, N. Silvestri, G. Pugliese, S. Nitti, L. Manna and T. Pellegrino, $Co_xFe_{3-x}O_4$ Nanocubes for Theranostic Applications: Effect of Cobalt Content and Particle Size, *Chem. Mater.*, 2016, **28**, 1769–1780, DOI: 10.1021/acs.chemmater.5b04780.

19 D. Polishchuk, N. Nedelk, S. Solopan, A. Ś. Waniewska, V. Zamorskyi, A. Tovstolytkin and A. Belous, Profound Interfacial Effects in $CoFe_2O_4/Fe_3O_4$ and $Fe_3O_4/CoFe_2O_4$ Core/Shell Nanoparticles, *Nanoscale Res. Lett.*, 2018, **13**, 67, DOI: 10.1186/s11671-018-2481-x.

20 X. Li and C. Kutal, Synthesis and characterization of superparamagnetic $Co_xFe_{3-x}O_4$ nanoparticles, *J. Alloys Compd.*, 2003, **349**, 264–268, DOI: 10.1016/s0925-8388(02)00863-0.

21 D. K. Tung, D. H. Manh, P. T. Phong, L. T. H. Phong, N. V. Dai, D. N. H. Nam and N. X. Phuc, Structural and magnetic properties of mechanically alloyed $Fe_{50}Co_{50}$ nanoparticles, *J. Alloys Compd.*, 2015, **640**, 34–38, DOI: 10.1016/j.jallcom.2015.04.022.

22 M. H. Phan, J. Alonso, H. Khurshid, P. L. Kelley, S. Chandra, K. S. Repa, Z. Nemati, R. Das, O. Iglesias and H. Srikanth, Exchange bias effects in iron oxide-based nanoparticle systems, *Nanomaterials*, 2018, **6**(11), 221, DOI: 10.3390/nano6110221.

23 P. T. Phong, V. T. K. Oanh, T. D. Lam, N. X. Phuc, L. D. Tung, N. G. U. Y. E. N. T. K. Thanh and D. H. Manh, Iron Oxide Nanoparticles: Tunable Size Synthesis and Analysis in Terms of the Core–Shell Structure and Mixed Coercive Model, *J. Electron. Mater.*, 2017, **46**, 2533–2539, DOI: 10.1007/s11664-017-5337-8.

24 J. M. Byrne, V. S. Coker, S. Moise, P. L. Wincott, D. J. Vaughan, F. Tuna, E. Arenholz, G. van der Laan, R. A. D. Pattrick, J. R. Lloyd and N. D. Telling, Controlled cobalt doping in biogenic magnetite nanoparticles, *J. R. Soc., Interface*, 2013, **10**, 130–134, DOI: 10.1098/rsif.2013.0134.

25 D. H. Manh, P. T. Phong, T. D. Thanh, D. N. H. Nam, L. V. Hong and N. X. Phuc, Size effects and interactions in La0.7Ca0.3MnO3 nanoparticles, *J. Alloys Compd.*, 2011, **509**, 1373, DOI: 10.1016/j.jallcom.2010.10.104.

26 D. Li, H. Yun, B. T. Diroll, V. V. T. Doan-Nguyen, J. M. Kikkawa and C. B. Murray, Synthesis and Size-Selective Precipitation of Monodisperse Nonstoichiometric $M_xFe_{3-x}O_4$ (M = Mn, Co) Nanocrystals and Their DC and AC Magnetic Properties, *Chem. Mater.*, 2016, **28**, 480–489, DOI: 10.1021/acs.chemmater.5b03280.

27 Y. Yu, A. M. Garcia, B. Ning and S. Sun, Cobalt-substituted magnetite nanoparticles and their assembly into ferromagnetic nanoparticle arrays, *Adv. Mater.*, 2013, **25**, 3090–3094, DOI: 10.1002/adma.201300595.

28 R. Sharma, P. Thakur, M. Kumar, N. Thakur, N. S. Negi, P. Sharma and V. Sharma, Improvement in magnetic behaviour of cobalt doped magnesium zinc nano-ferrites *via* co-precipitation route, *J. Alloys Compd.*, 2016, **684**, 569–581, DOI: 10.1016/j.jallcom.2016.05.200.

29 F. L. Deepak, M. B. López, E. C. Argibay, M. F. Cerqueira, Y. P. Redondo, J. Rivas, C. M. Thompson, S. Kamali, C. R. Abreu, K. Kovnir and Y. V. Kolenko, A Systematic Study of the Structural and Magnetic Properties of Mn, Co, and Ni-Doped Colloidal Magnetite Nanoparticles, *J. Phys. Chem. C*, 2015, **119**, 11947–11957, DOI: 10.1021/acs.jpcc.5b01575.

30 H. Topsøe, J. A. Dumesic and M. Boudart, Mössbauer spectra of stoichiometric and nonstoichiometric Fe_3O_4 microcrystals, *J. Phys. Colloq.*, 1974, **35**, C6–C411, DOI: 10.1051/jphyscol:1974680.

31 T. K. McNab, R. A. Fox and A. J. F. Boyle, Some Magnetic Properties of Magnetite (Fe_3O_4) Microcrystals, *J. Appl. Phys.*, 1968, **39**, 5703, DOI: 10.1063/1.1656035.

32 T. C. Gibb, *Principles of Mössbauer Spectroscopy*, Chapman and Hall, London 1976.

33 M.-H. Phan, J. Alonso, H. Khurshid, P. L. Kelley, S. Chandra, K. S. Repa, Z. Nemati, R. Das, Ó. Iglesias and H. Srikanth, Exchange Bias Effects in Iron Oxide-Based Nanoparticle Systems, *Nanomaterials*, 2016, **6**, 221, DOI: 10.3390/nano611022.

34 T. L. Phan, N. Tran, D. H. Kim, N. T. Dang, D. H. Manh, T. N. Bach, C. L. Liu and B. W. Lee, Magnetic and Magnetocaloric Properties of $Zn_{1-x}Co_xFe_2O_4$ Nanoparticles, *J. Electron. Mater.*, 2017, **46**, 4214–4226, DOI: 10.1007/s11664-017-5359-2.

35 V. Mameli, A. Musinu, A. Ardu, G. Ennas, D. Peddis, D. Niznansky, C. Sangregorio, C. Innocenti, N. T. K. Thanh and C. Cannas, *Nanoscale*, 2016, **8**, 10124–10137, DOI: 10.1039/C6NR01303A.

36 M. Blume and J. A. Tjon, Mössbauer Spectra in a Fluctuating Environment, *Phys. Rev.*, 1968, **165**, 446, DOI: 10.1103/PhysRev.165.446.

37 A. E. Deatsch and B. A. Evans, Heating efficiency in magnetic nanoparticle hyperthermia, *J. Magn. Magn. Mater.*, 2014, **354**, 163–172, DOI: 10.1016/j.jmmm.2013.11.006.

38 R. Hergt, S. Dutz, R. Muller and M. Zeisberger, Magnetic particle hyperthermia: nanoparticle magnetism and materials development for cancer therapy, *J. Phys.: Condens. Matter*, 2006, **18**, S2919, DOI: 10.1016/0953-8984/18/38/S26.

39 D. H. Manh, P. T. Phong, P. H. Nam, D. K. Tung, N. X. Phuc and In-Ja Lee, Structural and magnetic study of $La_{0.7}Sr_{0.3}MnO_3$ nanoparticles and AC magnetic heating characteristics for hyperthermia applications, *Physica B*, 2014, **444**, 94–102, DOI: 10.1016/j.physb.2014.03.025.

40 R. Hiergeist, W. AndraK, N. Buske, R. Hergt, I. Hilger, U. Richter and W. Kaiser, Application of magnetite ferrofluids for hyperthermia, *J. Magn. Magn. Mater.*, 1999, **201**, 420–422, DOI: 10.1016/S0304-8853(99)00145-6.